Trifunctional Fishbone-like PtCo/Ir Enables High-Performance Zinc-Air Batteries to Drive the Water-Splitting Catalysis

Yingjun Sun[a,b#], Bolong Huang[c#], Yingjie Li[a], Yi Xing[a], Mingchuan Luo[a], Chunji Li[a], Yingnan Qin[a,b], Lei Wang[b] and Shaojun Guo[a,d,e]*

[a]Department of Materials Science & Engineering, College of Engineering, Peking University, Beijing, 100871, China.

[b]College of Chemistry and Molecular Engineering, Qingdao University of Science and Technology, Qingdao 266042, China.

[c]Department of Applied Biology and Chemical Technology, The Hong Kong Polytechnic University, Hung Hom, Kowloon 999077, Hong Kong SAR.

[d]BIC-ESAT, College of Engineering, Peking University, Beijing, 100871, China.

[e]Department of Energy and Resources Engineering, College of Engineering, Peking University, Beijing, 100871, China.

[#]These authors contributed equally
*E-mail: guosj@pku.edu.cn

Abstract

Precise tuning of the geometric and electronic structure of Pt- or Ir-based nanomaterials is pivotal for the development of highly efficient catalysts of hydrogen evolution reaction (HER), oxygen reduction reaction (ORR) and oxygen evolution reaction (OER). Indeed, alloying Pt or Ir with single metal as a common approach can modulate the d-band center for better performance. However, this strategy usually leads to single-functional high-performance nanocatalysts. Herein, we report a new class of Pt-rich PtCo/Ir-rich IrCo trimetallic fishbone-like nanowires (PtCo/Ir FBNWs) with tailored one-dimensional surface/interface structure for achieving remarkable trifunctional catalytic properties effectively tuned by *d-band* pinning and offsetting with morphological and compositional controls. Through such metallic hetero-*d*-band-junction mechanism, the optimal multi-functional performances have been robustly pinned via precise ternary alloying ratios. Particularly, as-made $Pt_{62}Co_{23}/Ir_{15}$ FBNWs exhibit outstanding electrocatalytic activities for HER and OER in both acid and alkaline solutions, exceeds that of commercial Pt/C or Ir/C, respectively. The overall water-splitting devices driven by $Pt_{62}Co_{23}/Ir_{15}$ FBNWs is applicable in wide pH medium,

which has achieved the current density of 13.3 mA cm^{-2} in acid electrolyte at a low potential of 1.55 V, 30.9 times outclassed that of Pt/C-Ir/C. Notably, the performance of Pt$_{62}$Co$_{23}$/Ir$_{15}$ FBNWs in ORR also maintain a higher level than Pt/C that can be utilized in high-performance zinc-air batteries to drive the water-splitting in a self-powered manner. Theoretical calculations reveal that their superior multifunctional catalytic activities can be attributed to the unique morphology induced interfacial stress, which can facilitate an effective combination of d-band pinning and offsetting for dynamically self-activations among HER, OER, and ORR catalysis.

Introduction

The significant issues emerging in the current energy crisis and environmental pollution have put forward major demands in searching for efficient and sustainable energy conversion devices. Representative innovative technologies are the electrocatalytic water-splitting process featuring hydrogen evolution reaction (HER) and oxygen evolution reaction (OER), and the rechargeable metal (zinc or lithium) air battery involving oxygen reduction reaction (ORR) and OER, and fuel cells involving ORR and hydrogen oxidation reaction (HOR). The practical applications of electrochemical reactions-relevant renewable energy systems are highly dependent on electrocatalysts. Although great efforts have been devoted to searching for high-performance catalysts, platinum (Pt) still has been considered as the optimal tri-functional electrocatalyst for the both the ORR and HOR in fuel cells as well as the HER in overall water-splitting. For the utilization in all pH environment, Iridium (Ir) is one of the rising stars for OER. However, the sluggish reaction kinetics of the reported catalysts still hinder their further commercialization. Alloying the Pt (Pt-5$d^{8\sim9}$) or Ir (Ir-5d^7) with a 3d transition metal (such as Co-3d^7) is an effective strategy to overcome this obstacle, as the electronic structure of resultant alloy catalysts can be modified by the alloy inducd orbital overlapping near the surface active sites. That is, an optimal state can be established through the varied distribution of d-electron and adsorption strength on noble metal by alloy effect. Unfortunately, previous studies of Pt or Ir-based bimetallic catalysts can only promote a certain catalytic reaction, which results in that the preferred HER (ORR) catalysts with poor OER performance and vice versa. Consequently, preparing the "omnipotent" catalysts towards HER, ORR and OER in the water splitting and metal-air batteries concurrently remains an open challenge.

Herein, a class of Pt-rich PtCo/Ir-rich IrCo trimetallic interface fishbone-like nanowires

(FBNWs) have been successfully synthesized and applied as highly efficient trifunctional and environmentally universal electrocatalysts for boosting the performance of overall water-splitting and metal-air batteries. The PtCo/Ir NWs show the composition-dependent electrocatalytic activity, in which the $Pt_{62}Co_{23}/Ir_{15}$ FBNWs exhibit the highest HER and OER activities in wide pH conditions, superior to that of typical Pt/C-Ir/C system. Impressively, the $Pt_{62}Co_{23}/Ir_{15}$ FBNWs as highly efficient catalyst for the overall water-splitting, it endows great potential in the self-powered zinc-air battery systems or the assembled lithium-air batteries. More importantly, DFT calculations demonstrate that the design of multi-functional catalyst system with ultrahigh robustness can be achievable based on the d-band pinning general mechanism. With exceptionally highly electron-active Ir-5d modulations, the overall morphology is not only flexibly tuned towards the substantially high active area, but also contributes di-valence-state of Pt-site for dynamically self-activated redox switching as well as lower valence Co-site, contributing to excellent water adsorption and splitting kinetics. With such Ir-tuned metallic interface region, Pt-based hetero-*d-band*-junction is contributed in this community with robustly pinning Co^0/Co^{2+} as an electron-rich center towards universal catalysis.

Results and discussion

Structural and Morphology Characterization

In a typical synthesis of PtCo/Ir FBNWs, platinum(II) acetylacetonate (Pt(acac)$_2$), iridium(II) 2,4-pentanedionate (Ir(acac)$_2$), cobalt(III) acetylacetonate (Co(acac)$_3$), celyltrimethylammonium chloride (CTAC), glucose and oleylamine (OAm) were mixed into a glass vial and ultrasonicated for 1 h. The resultant mixture was then heated to 220 °C and maintained at that temperature for 5 h (see Supporting Information for details). The black product was first characterized by low-magnification transmission electron microscopy (TEM) and high-angle annular dark-field scanning TEM (HAADF-STEM). As shown in **Figure 1a&Figure S1**, the product has uniform 1D morphology with a length of hundreds of nanometers that gives rise to a high aspect ratio of ~30. TEM image (**Figure 1b**) exhibits that each NW consists of abundant thorns-like fishbone with an average diameter of 20 nm (*inset* of **Figure 1b**). The powder X-ray diffraction (PXRD) pattern of PtCo/Ir FBNWs (**Figure 1c**) shows the typical face-centered cubic (*fcc*) structure. The molar ratio of Pt/Co/Ir is determined to be 66/18/16 by the TEM energy-dispersive X-ray spectroscopy (TEM-EDS) (**Figure 1d**), being in accordance with the result from inductively coupled plasma-atomic emission spectroscopy (ICP-AES)

(62/23/15). The STEM-EDS mapping technique is used to further determine the distribution of Pt, Co and Ir within FBNWs, in which Ir (red) element is mostly distributed around the fishbone edge and Pt (green) element is distributed mainly along the central skeleton, indicating the existence of interface between PtCo and IrCo (**Figure 1e**). The linear scan profile further confirms that the PtCo/Ir FBNW (*inset* of **Figure 1f**) is characteristic of a Pt-rich PtCo skeleton and an Ir-rich IrCo edge (**Figure 1f**). **Figure 1g** shows the spherical aberration corrected STEM image along the [110] zone axis. The surface of the FBNW is rough and has a high density of atomic steps, which is the key to enhancing catalytic performance (**Figure S2**).

We further investigated the growth process and formation mechanism of the PtCo/Ir FBNWs (**Figure 2a-i**). At the initial 1 h reaction stage, the atomic-thick Pt NWs were obtained (**Figure 2a, b**), followed by forming the rough PtCo NWs at 3 h stage (**Figure 2c-f**), as confirmed by PXRD (**Figure 2l**) and TEM-EDS (**Figure S3**). When the reaction time was increased to 4 h, the bones areas became tapering (**Figure 2g, h**). The molar ratio of Pt/Co/Ir changes from 76/24/0 at 3 h to 71/19/10 at 4 h, suggesting that the Ir precursors are reduced during this period. The final composition of Pt/Co/Ir is maintained at about 62/23/15 at 5 h (**Figure 2i, j**), and it shows almost no variation even if the reaction time is extended to 8 h (61/23/16) (**Figure 2k**). Therefore, the growth of PtCo/Ir FBNWs primarily involves the formation of PtCo NWs due to the reduction of Pt and Co precursors within the first three hours, followed by the reduction of Ir precursors on the edge of preformed PtCo NWs (**Figure 2m**). The content of Ir in FBNWs can be finely tuned by altering the amount of Ir precursors (**Figure S4**). Only rough $Pt_{79}Co_{21}$ NWs with 12.6 nm diameter were obtained in the absence of $Ir(acac)_2$ (**Figure S4a, b**). By increasing the amount of Ir precursor to 4.0, 8.0 and 16.0 mg, the edge and diameter of the PtCo/Ir FBNWs become thinner and larger, and the corresponding composition turns to be $Pt_{65}Co_{27}/Ir_8$, $Pt_{62}Co_{23}/Ir_{15}$ and $Pt_{50}Co_{24}/Ir_{26}$, respectively (**Figure S4c-h**). There is no noticeable change in morphology when the amount of $Ir(acac)_2$ was further increased to 20.0 mg (**Figure S5**). Furthermore, XRD results show that the diffraction peaks shift towards higher 2θ values with increasing the Ir content (**Figure S6**).

HER and OER performances in acid and alkaline electrolytes.

The hydrogen evolution reaction (HER) and oxygen reduction reaction (OER) catalyzed by the as-prepared PtCo/Ir FBNWs and PtCo NWs were first investigated in 0.1 M $HClO_4$ solution at a scan rate of 5 mVs^{-1} (**Figure 3a, b**). Before the HER test, the PtCo/Ir FBNWs and PtCo NWs were

supported on Vulcan XC72R carbon and then subject to thermal annealing to remove the surfactant around the surface. **Figure 3a** shows the HER polarization curves of different catalysts. The $Pt_{62}Co_{23}/Ir_{15}$ FBNWs/C exhibits a highest current density of 45.7 mA cm^{-2} at an overpotential of 18 mV, 6.49 and 7.76 times higher than those of $Pt_{79}Co_{21}$ NWs/C (7.04 mA cm^{-2}) and Pt/C (5.89 mA cm^{-2}), respectively. Furthermore, PtCo/Ir FBNWs/C exhibits significantly improved kinetics relative to $Pt_{79}Co_{21}$ NWs/C and Pt/C. The Tafel slope of $Pt_{62}Co_{23}/Ir_{15}$ FBNWs/C is about 24.2 mV dec^{-1}, lower than either that of $Pt_{79}Co_{21}$ NWs/C (29.7 mV dec^{-1}) or Pt/C (31.6 mV dec^{-1}), indicating its fast kinetics (*inset* of **Figure 3a**). The overpotential of $Pt_{62}Co_{23}/Ir_{15}$ FBNWs/C at 10 mA cm^{-2} is around 14 mV, lower than those of other PtCo/Ir compositions (16 mV for $Pt_{50}Co_{24}/Ir_{26}$ FBNWs/C and 17 mV for $Pt_{65}Co_{27}/Ir_{8}$ FBNWs/C) and Pt/C (23 mV). The overpotentials of different catalysts at a current density of 10 mA cm^{-2} and 20 mA cm^{-2} are summarized in **Figure S7**. The TOF of different catalysts (determined by normalizing current density to the total mass of catalysts at the overpotential of 20 mV) is shown in the left of **Figure 3c**. The $Pt_{62}Co_{23}/Ir_{15}$ FBNWs/C exhibits the highest TOF values of 3.62 s^{-1}, 8.3 times higher than that of Pt/C, respectively. The durability of the $Pt_{62}Co_{23}/Ir_{15}$ FBNWs/C was further evaluated by using accelerating durability test at the scan rate of 100 mV s^{-1}. There is almost no change in polarization curves of the $Pt_{62}Co_{23}/Ir_{15}$ FBNWs/C before and after 5000 cycles (**Figure S8**). We find that, in 0.1 M KOH solution, the HER performance of various catalysts follows the same order with that in acid solution: $Pt_{62}Co_{23}/Ir_{15}$ FBNWs/C > $Pt_{50}Co_{24}/Ir_{26}$ FBNWs/C > $Pt_{65}Co_{27}/Ir_{8}$ FBNWs/C > $Pt_{79}Co_{21}$ NWs/C > Pt/C (**Figure S9**). The $Pt_{62}Co_{23}/Ir_{15}$ FBNWs/C still shows the lowest overpotential of 24 mV at 10 mA cm^{-2} and highest TOF value of 0.56 s^{-1} with the Tafel slope of 43.0 mV dec^{-1}.

The linear sweep voltammetry (LSV) curves of PtCo/Ir FBNWs were further used to evaluate the oxygen evolution reaction (OER) activity in O_2-saturated 0.1 M $HClO_4$ with a scan rate of 5 mV s^{-1} (**Figure 3b**). Obviously, the PtCo/Ir FBNWs/C has a significant OER enhancement compared with Ir/C. The optimized $Pt_{62}Co_{23}/Ir_{15}$ FBNWs/C only requires an overpotential of 308 mV to achieve the current density of 10 mA cm^{-2}, lower than those of other PtCo/Ir FBNWs/C with different compositions (310 mV for $Pt_{50}Co_{24}/Ir_{26}$ FBNWs/C and 330 mV for $Pt_{65}Co_{27}/Ir_{8}$ FBNWs/C), Ir/C (380 mV) and $Pt_{79}Co_{21}$ NWs/C (560 mV), respectively (**Figure S10**). The $Pt_{62}Co_{23}/Ir_{15}$ FBNWs/C also shows the smallest Tafel slope of 52.2 mV dec^{-1} (*inset* of **Figure 3b**), indicating alloying with Ir can efficiently enhance the OER kinetics. To study the intrinsic activity, the TOF

values of various catalysts are calculated from the current at an overpotential of 300 mV (1.53 V), which follow the sequence of $Pt_{62}Co_{23}/Ir_{15}$ FBNWs/C > $Pt_{50}Co_{24}/Ir_{26}$ FBNWs/C > $Pt_{65}Co_{27}/Ir_8$ FBNWs/C > Ir/C > $Pt_{79}Co_{21}$ NWs/C. The TOF of $Pt_{62}Co_{23}/Ir_{15}$ FBNWs/C reaches 0.58 s^{-1}, 19.2 and 4.5 times higher than those of $Pt_{79}Co_{21}$ NWs/C and Ir/C catalysts (right of **Figure 3c**). The catalytic durability of the $Pt_{62}Co_{23}/Ir_{15}$ FBNWs/C was examined by 5000 potential cycles between 1.2 and 1.6 V *vs.* reversible hydrogen electrode (RHE) in 0.1 M HClO$_4$. **Figure S11** shows the polarization curves of $Pt_{62}Co_{23}/Ir_{15}$ FBNWs/C before and after 5,000 cycles. When switching to 0.1 M KOH electrolyte, the $Pt_{62}Co_{23}/Ir_{15}$ FBNWs/C still shows the highest TOF of 0.52 s^{-1} and lowest Tafel slope of 67 mV dec^{-1} among all the prepared catalysts (**Figure S12**).

Overall water splitting catalysis

Based on remarkable HER and OER catalytic performances of PtCo/Ir FBNWs/C catalysts, we make an electrolyzer in a two-electrode cell by using PtCo/Ir FBNWs/C as the efficient bifunctional electrocatalysts. The as-prepared PtCo/Ir FBNWs supported on a carbon fiber paper (CFP) are used for both anode and cathode. As a control, commercial Pt/C and Ir/C on CFP serve as cathode and anode (Pt/C-Ir/C), respectively. **Figure 3d** shows the polarization curves of PtCo/Ir FBNWS/CFP, $Pt_{79}Co_{21}$ NWs/CFP and Pt/C-Ir/C for overall water splitting in 0.1 M HClO$_4$ at a scan rate of 5 mV s^{-1}. The $Pt_{62}Co_{23}/Ir_{15}$ FBNWs/CFP exhibits the highest activity with the need of a cell voltage of 1.5 V to afford 5 mV cm^{-2}. The vigorous gas evolutions on both electrodes are shown in the *inset* of **Figure 3d**. The current density of $Pt_{62}Co_{23}/Ir_{15}$ FBNWs/CFP can reach 13.3 mA cm^{-2} at overall water splitting cell voltage of 1.55 V in 0.1 M HClO$_4$, 51.2 and 30.9 times higher than those of $Pt_{79}Co_{21}$ NWs/CFP (0.26 mA cm^{-2}) and Pt/C-Ir/C (0.43 mA cm^{-2}), respectively. The stability of $Pt_{62}Co_{23}/Ir_{15}$ FBNWs/CFP and Pt/C-Ir/C toward the overall water-splitting was further evaluated by cycling the potential between 1.25 and 1.65 V *vs.* RHE for 10,000 cycles (**Figure 3e**). The polarization curve of $Pt_{62}Co_{23}/Ir_{15}$ FBNWs/CFP shifts only 3 mV at 10 mA cm^{-2} after long-term stability test, while a rapid descent occurs on Pt/C-Ir/C. These results reveal that $Pt_{62}Co_{23}/Ir_{15}$ FBNWs have the robust durability for overall water-splitting catalysis in acidic solution.

The overall water splitting performances of the $Pt_{62}Co_{23}Ir_{15}$ FBNWs catalyst in alkaline and neutral media were also investigated (**Figure S13**). The $Pt_{62}Co_{23}/Ir_{15}$ FBNWs exhibit better performance (onset potential of 1.5 V in alkaline solution and 1.54 V in neutral solution, respectively)

than those of the Pt/C-Ir/C catalysts. These prove that alloying appropriate Ir elements on the edge of PtCo NWs can efficiently enhance the water splitting performance in a wide pH range.

Metal-air batteries

The optimized $Pt_{62}Co_{23}/Ir_{15}$ FBNWs/C also shows extraordinary ORR performance in alkaline solution. Its ORR mass and specific activities are 0.83 A cm^{-2} and 1.33 mA cm^{-2} (**Figure S14a, b**), about 4.6 and 5.3 times higher than those of Pt/C, respectively. Furthermore, they deliver a charge/discharge voltage gap of 0.65 V (a discharge potential of 1.28 V and a charge potential of 1.93 V) at 5 mA cm^{-2} for Zinc-air battery, much lower than that of the 20% Pt/C and IrO$_2$ catalyst (**Figure S14c**). A self-powered electrochemical water-splitting system by zinc-air battery was then demonstrated by integrating the unique electrocatalytic activity of HER with OER. One rechargeable zinc-air battery connected in series using the trifunctional $Pt_{62}Co_{23}/Ir_{15}$ FBNWs catalyst were integrated with a water-splitting cell (**Figure 3f**). Hydrogen and oxygen bubble generation were observed on the two electrodes (**Movie S1**), indicative of the successful operation and high efficiency of this self-powered system. The $Pt_{62}Co_{23}/Ir_{15}$ FBNWs/C also worked well as the excellent catalysts for developing high-performance lithium-air batteries (**Figure S15**).

Calculation

Considering the formation mechanism, the theoretical model of core/shell layered structure has been built with a side-chain branch established for modifying the interface (IF) electronic structures (**Figure 4a**). The surface unit cell shows Pt and Co can co-exist in both IF and side-chain, respectively, while the Ir distributes within the inner boundary as shell and side-chain. The real spatial orbitals of bonding and anti-bonding states near the Fermi level (E$_F$) denote the most active electrons are enriched and localized near the Co-sites (**Figure 4b**). The two-dimensional electron differential density distribution indicates the Co-sites gain electrons can act as the electron-agglomeration bath while the Ir and Pt sites serve as electron-depletion centers to actively pin the potentially existing Co^0 state near the IF region (**Figure 4c**). The projected partial density of states (PDOSs) demonstrates the subtle interplay of Pt, Ir, and Co sites, respectively. The PDOS shows similar attribution for the Pt-site at side-chain and Pt bulk metal, which is evidently different from Pt-site within IF region. The Pt-dominated initial adsorption behaviors for H and O-species would be potentially enhanced due to the shift of Pt-4d band center towards E$_F$ from E$_V$-3.5 eV

(side-chain) to E_V-2.2 eV (IF) (**Figure 4d**). The Ir sites at the side-chain and shell regions display similar electronic character with the high lying positions of Ir-5d band centers at E_V-1.9 eV. Differently, the 5d-band center of Ir bulk metal state are staying much lower at E_V-4.0 eV. Thus, this indicates the Ir-sites within the PtCo/Ir FBNWs system are firmly playing as an apparent electronic depletion center (**Figure 4e**). Compare with the Co bulk metal states, the Co-sites at the IF and side-chain regions also show similar electron-rich character. The modified Co-3d band centers have been downshifted from the E_V-1.4 eV (bulk metal) to E_V-2.2 eV (side-chain and IF regions), respectively. This generally supports the existence of lower valence state like Co^0 or Co^{2+} responsible for efficient water splitting catalysis (**Figure 4f**).

We further move on to the energetic perspective to elucidate the catalytic reactivity. For HER, the overall reaction performs a rather favorable level of ΔG=-1.82 eV. As taken the itinerant state for reference, the initial adsorption of H_2O determined overall evolution path will nearly undergo an effective electron-transfer reaction exothermically (**Figure 5a**). On the other hand, the water-splitting ability was an essential factor to control the overall HER rate is also prominent with very low barrier height. The transition state (TS) barrier height possesses 0.40 eV and performs as superior as the NiMoP system by Ren *et al* [Nano Energy 53 (2018) 492–500] or $MoNi_4$ modified MoO_2 system by Feng *et al* [Nat. Commun. 8, 15437 (2017)]. The overall ΔG (-0.68 eV) also guarantees a weakened binding for effective transformation of intermediates (**Figure 5b**). Formation energies also exhibit the favorable adsorption of H, 2H and a relatively weaker H_2 to prevent the overbinding effect (**Figure 5c**). The chemisorption energy further indicates the HER can proceed efficiently as the H-chemisorption approaches the thermoneutral line (ΔG=0 eV). The H_2 will desorb easily since it reflects the positive chemisorption energy (**Figure 5d**).

Further on the energetic pathway of OER, at the U=0 V, the initial H_2O adsorption preferred the Co-site near the IF region, which recalls the lower valence state observed for Co-site at the IF region of this system. The OH^- group is two-fold coordinated and the splitting process is energetically promoted by the combination of Co-Pt sites or Pt-Pt site. This configuration follows the trend of increased electronic activities of Pt site. The initial water splitting step is the potentially determining step, wherein the barrier decides the overall overpotential (*i.e.* max {[barrier-1.23 eV]/e}) with the value of 0.102 eV. This can also be found from the energy evolutions at the electrode potential of U=1.23 V. With the synergetic contribution of different electronic activities of Pt-Co-Ir sites, the

overbinding effect of following steps of transforming intermediates of O-species are thus alleviated to lower than the initial water splitting step with relatively small uphill barriers (**Figure 5e**). For the ORR steps, optimal oxygen adsorption energy determines the overall pathway. Pure Pt (111) surface exhibits stronger adsorption while the second reduction step of forming OOH is potentially overbid. Owing to this rather low energy step, the consequent reduction steps are energetically uphill to meet the average overpotential of 0.85 V. In contrast, the PtCo/Ir system has overall attenuated the reduction uphill barriers. Moreover, the final production step displays an energetic downhill trend. This optimal performance arises because the higher electronic activities of Ir and lower valence Co-site weaken the over-binding effect of Pt-O for the initial O-adsorption (**Figure 5f**). With the detailed discussion from electronic and energetic perspectives, we further proved that this PtCo/Ir IF system possesses high electronic activities and can fulfill the dynamically self-activating performance for the wide spectrum of HER, OER and ORR energetic performance simultaneously.

Conclusion

In summary, we demonstrate the synthesis and characterization of a novel class of tri-functional Pt-rich PtCo/Ir-rich IrCo interface FBNWs for boosting three key electrocatalytic reactions HER, OER and ORR in water splitting, fuel cells, and metal-air batteries. The $Pt_{62}Co_{23}/Ir_{15}$ FBNWs show the optimal performance of both HER and OER activities in acid and alkaline solutions, far exceeding the commercial Pt/C or Ir/C, and therefore can be applied in a high-performance water electrolyzer at all pH values. The interesting trifunctional properties of FBNWs endow them to develop high-performance zinc-air batteries to drive the overall water-splitting in a self-power manner. DFT calculations has unravelled that the highly electron-active Ir-5d orbital modulations is vital to the pure metallic Pt-based hetero-*d-band*-junction to realize the general ultrahigh robustness of switchable redox cycles. Therefore, a broad range of applications of this PtCo/Ir interface system can be expected based on its high electronic activities as well as the dynamically self-activating catalytic reactivity. This work will insightfully guide the direction of effective modulation of the *d-band* pinning and offsetting with morphological and compositional controls.
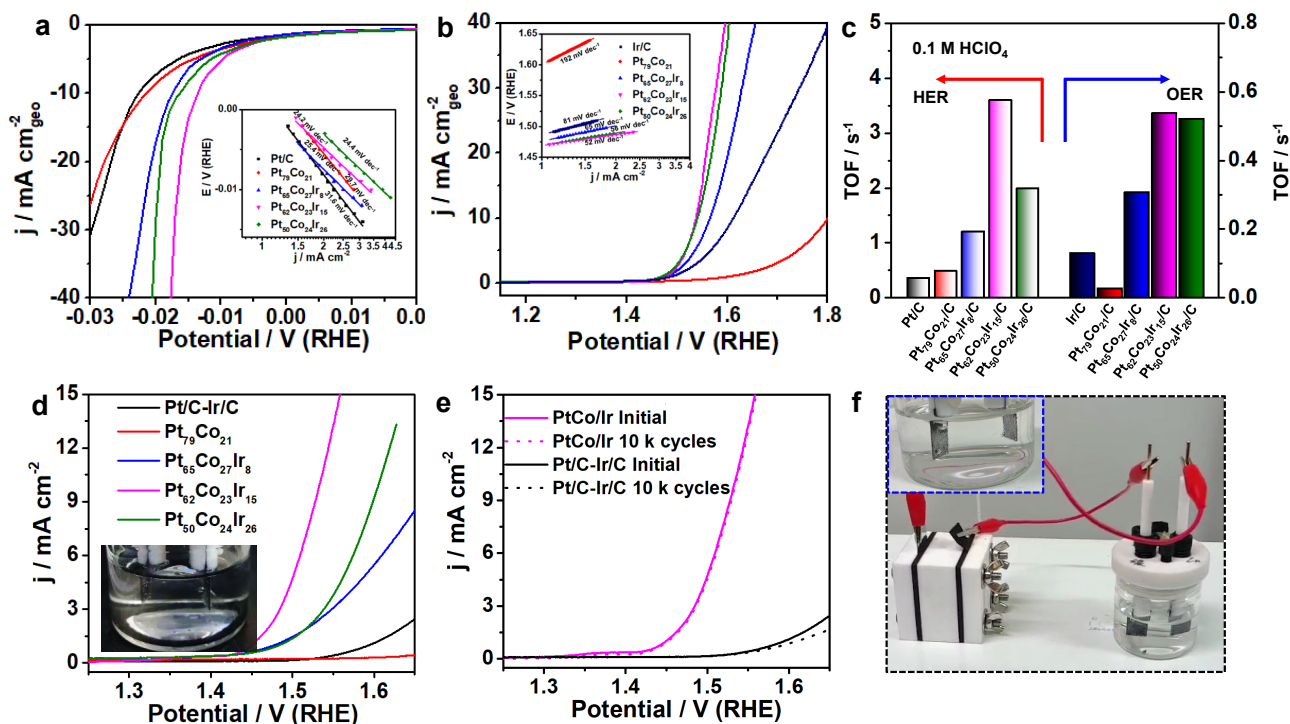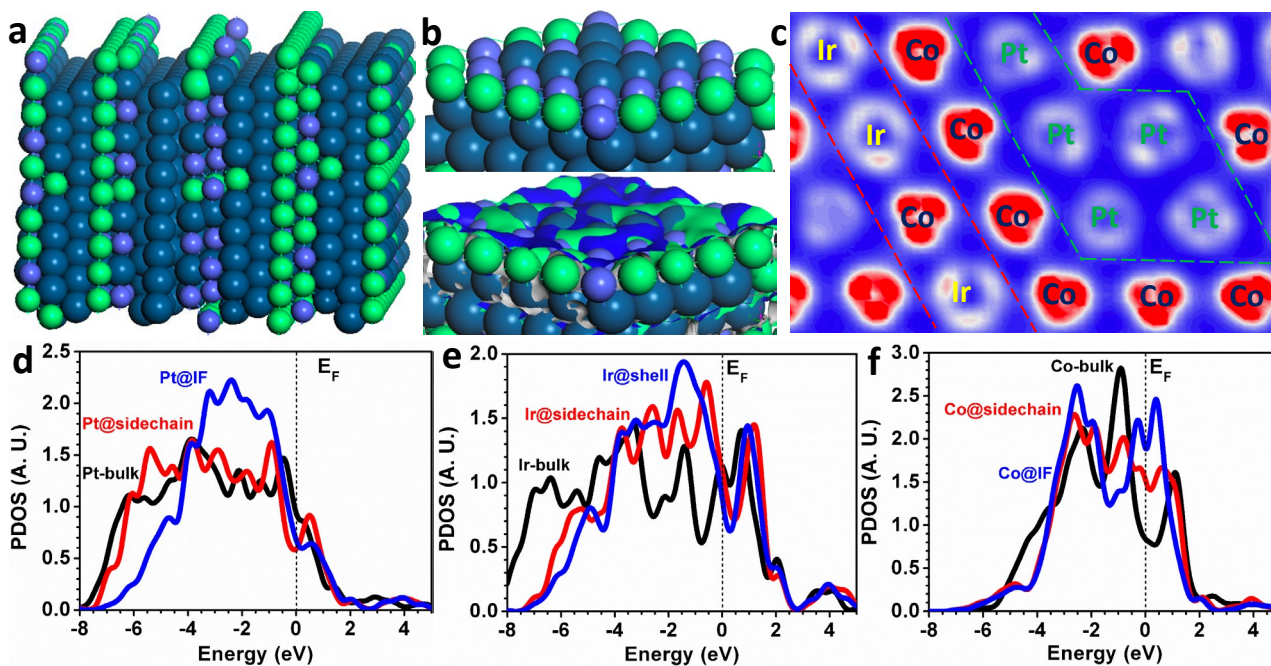
Figures
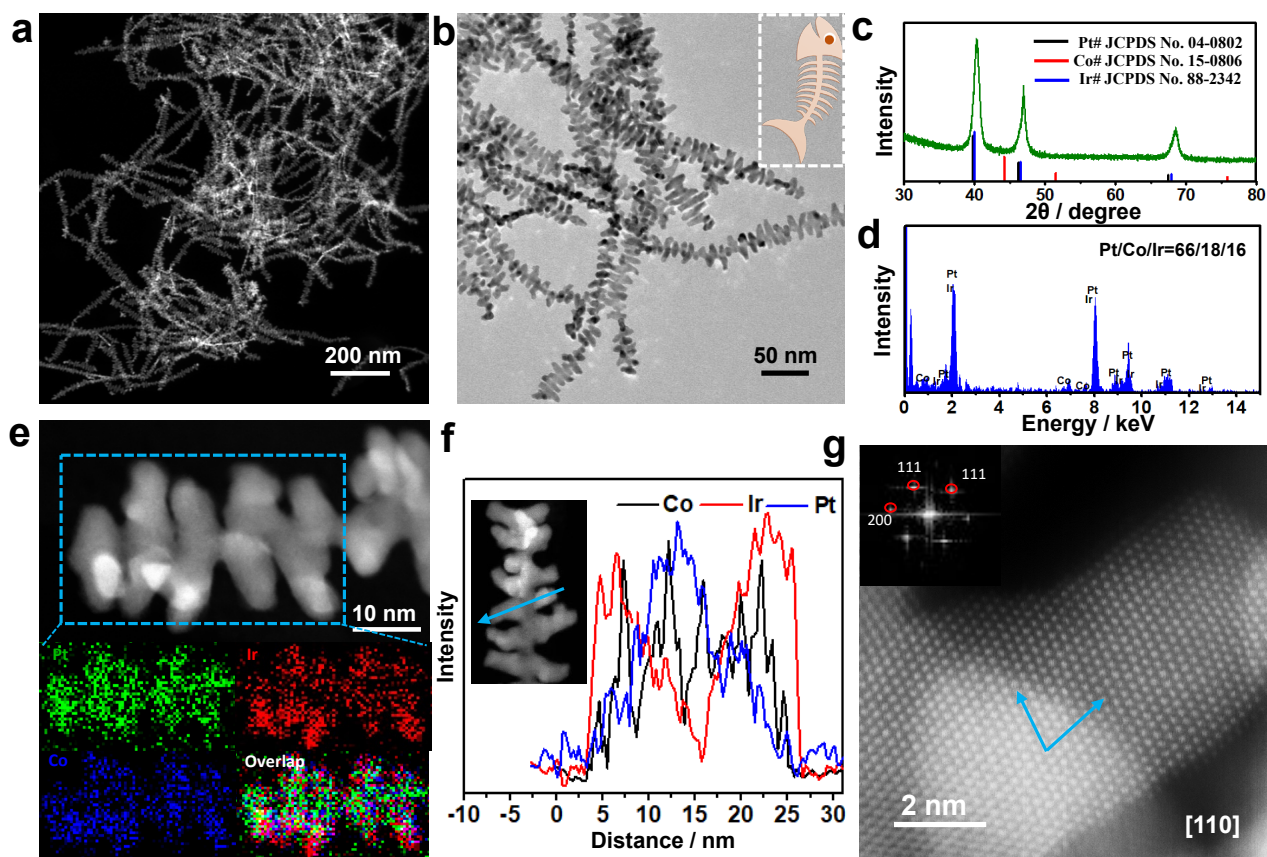
Figure 1. Structural and compositional characterization of PtCo/Ir FBNWs. Representative (**a**) low-magnification HAADF-STEM image, (**b**) high-magnification TEM image, (**c**) PXRD pattern, (**d**) TEM-EDS, (**e**) STEM-EDS elemental mapping, (**f**) line scan, (**g**) atomic resolution HAADF-STEM image of PtCo/Ir FBNWs. The *inset* in (**f**) is STEM image of a single FBNW. The *inset* in (**g**) is FFT pattern of PtCo/Ir FBNWs.
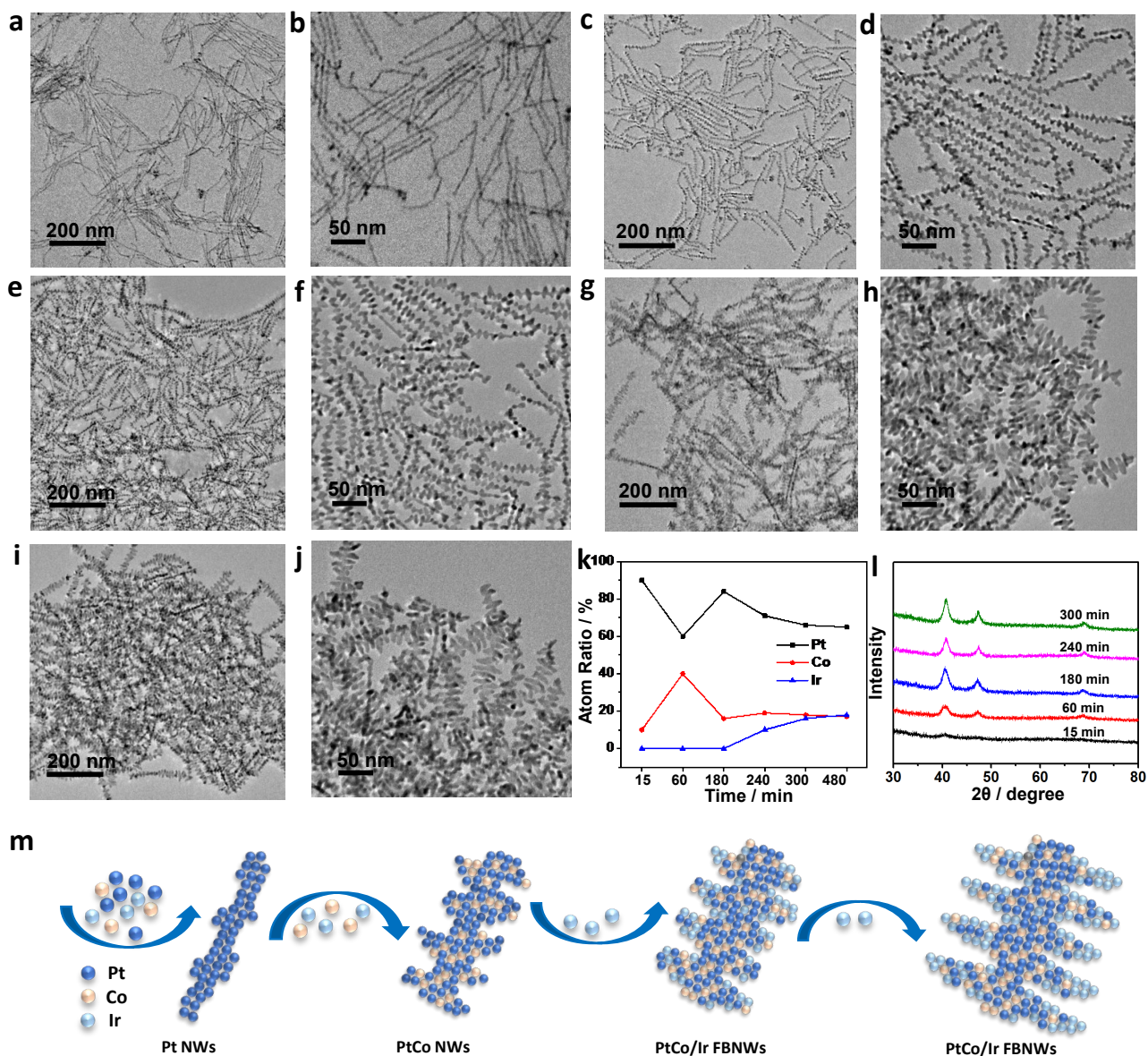
Figure 2. Formation mechanism of PtCo/Ir FBNWs. Representative TEM images of PtCo/Ir FBNWs intermediates collected from (**a, b**) 15 min, (**c, d**) 60 min, (**e, f**) 180 min, (**g, h**) 240 min, (**i, j**) 300 min. (**k**) The changes on the composition ratio of Pt, Co and Ir for PtCo/Ir FBNWs intermediates, as determined by TEM-EDS measurements. (**l**) PXRD patterns of PtCo/Ir FBNWs intermediates collected from the reactions at different reaction times. (**m**) The schematic shows the formation mechanism of PtCo/Ir FBNWs.

Figure 3. Electrocatalytic performance of various catalysts. (**a**) HER polarization curves, (**b**) OER polarization curves and (**c**) TOF values of PtCo/Ir FBNWs/C, PtCo NWs/C, commercial Pt/C and Ir/C in 0.1 M HClO$_4$ solution. (**d**) Polarization curves of PtCo/Ir FBNWs/CFP, PtCo NWs/CFP and Pt/C-Ir/C for overall water splitting in 0.1 M HClO$_4$ solution at a scan rate of 5 mV s^{-1}. (**e**) Polarization curves of Pt$_{62}$Co$_{23}$Ir$_{15}$ FBNWs/CFP and Pt/C-Ir/C for overall water-splitting after 10,000 cycles. (**f**) A photograph shows an acid water splitting cell powdered by one zinc-air battery (top) and the electrocatalytic evolution of H$_2$ (right) and O$_2$ (left) bubbles (down). The *insets* in (a) and (b) are Tafel slopes of various catalysts towards HER and OER, respectively. The *inset* in (d) is the photograph of water-splitting device at working conditions.

Figure 4. (**a**) Side view of atomic configuration of overall model of PtCo/Ir catalyst system. (**b**) The surface of the core/shell IF region of the PtCo/Ir catalyst (higher-panel). The 3D real spatial orbital contour plots for the bonding and anti-bonding orbital near the E_F (lower-panel). (**c**) The charge density difference distribution has been illustrated on the localization of electrons in 2D slices. (**d**) PDOSs of the Pt-4d bands for the Pt site from bulk metal state, side-chain and IF region of this system. (**e**) PDOSs of the Ir-5d bands for the Ir site from the bulk metal state, side-chain and shell region of this system. (**f**) PDOSs for the Co-3d bands for Co site from the bulk metal state, side-chain and IF region of this system.
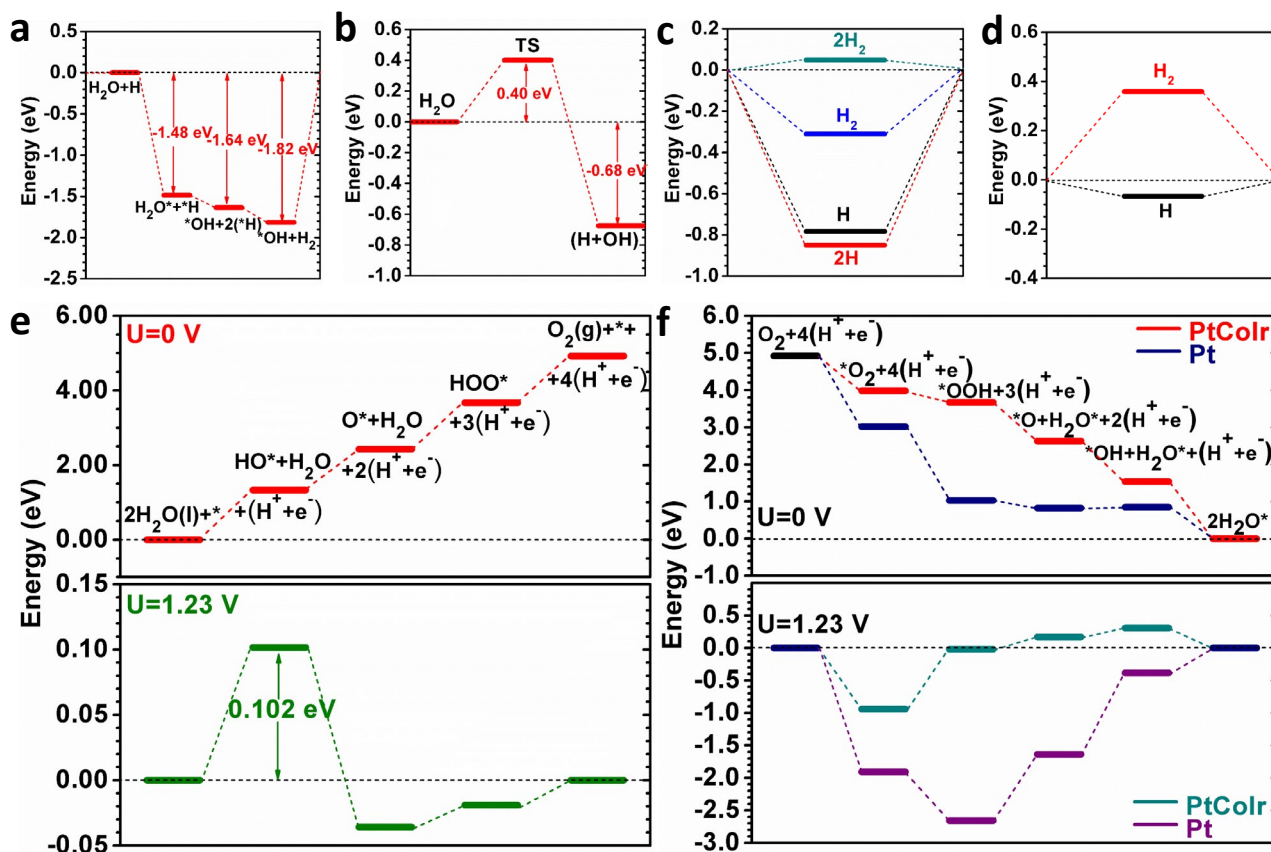
Figure 5. (**a**) The HER energetic pathway within alkaline condition. (**b**) The transition state barrier of H_2O splitting ability given by the PtCoIr system. (**c**) The adsorption formation energies of H, 2H, H_2 and $2H_2$, respectively. (**d**) The chemisorption energy of H and H_2 from the PtCoIr system. (**e**) The OER energetic pathway of PtCoIr system under U=0 and U=1.23 V electrode potentials, respectively. (**f**) The four-electron pathway for ORR under U=0 and U=1.23 V electrode potential, respectively.